

# A multiscale active nematic theory of microtubule/motor-protein assemblies

Tong Gao<sup>1</sup>, Robert Blackwell<sup>2</sup>, Matthew A. Glaser<sup>2</sup>, M. D. Betterton<sup>2</sup>, Michael J. Shelley<sup>1</sup>

<sup>1</sup>*Courant Institute of Mathematical Sciences,  
New York University, New York, NY 10012*

<sup>2</sup>*Department of Physics and Liquid Crystal Materials Research Center  
and Biofrontiers Institute University of Colorado, Boulder, CO 80309*

(Dated: May 17, 2022)

## Abstract

Microtubules and motor-proteins are the building blocks of self-organized subcellular structures such as the mitotic spindle and the centrosomal microtubule array. They are ingredients in new “bioactive” liquid-crystalline fluids that are powered by ATP, and driven out of equilibrium by motor-protein activity to display complex flows and defect dynamics. Here we develop a multiscale theory for such systems. Brownian dynamics simulations of polar microtubule ensembles, driven by active crosslinks, are used to study microscopic organization and the stresses created by microtubule interactions. This identifies two polar-specific sources of active destabilizing stress: polarity-sorting and crosslink relaxation. We develop a Doi-Onsager theory that captures polarity sorting, and the hydrodynamic flows generated by polar-specific active stresses. In simulating experiments of active flows on immersed surfaces, the model exhibits turbulent dynamics and continuous generation and annihilation of disclination defects. Analysis shows that the dynamics follows from two linear instabilities, and gives characteristic length- and time-scales.

The physics of biofilament sliding and polarity sorting by molecular motor constructs containing two or more active motors in active matter has been studied experimentally<sup>1-3</sup>. In earlier experiments, biofilaments were driven into static self-organized patterns such as vortices and asters, reminiscent of structures observed *in vivo*. Recently, in experiments of Sanchez *et al.*<sup>4</sup>, active networks were formed of microtubules (MTs) and synthetic multimeric kinesin-1 motor complexes with the aid of a depletant. In the presence of ATP, motor complexes can bind pairs of MTs and walk along MTs towards their plus-ends. When suspended in bulk, depletion interactions drove the formation of extended, highly ordered MT bundles characterized by bundle extension and fracture, and correlated with spontaneous large-scale fluid flows. When MT bundles were adsorbed onto an oil-water interface, they formed a dense, nematically ordered surface state and exhibited an active nematic phase characterized by the spontaneous generation and annihilation of disclination defect pairs.

Theoretical studies<sup>5-9</sup> have investigated aspects of these active-matter systems at different scales, from the dynamics and mechanical properties of filament bundles to macroscopic behavior and stability of active suspensions. Inspired by the experiments of Sanchez *et al.*<sup>4</sup>, both Giomi *et al.*<sup>10</sup> and Thampi *et al.*<sup>11</sup> have studied liquid crystal hydrodynamic models with fluid flow driven by an active stress<sup>12</sup>. In these rather general models the precise origins of the active stress driving the system are unidentified. Giomi *et al.* developed a theory for the speed at which defects move apart in active nematics, assuming the presence of a defect pair as an initial condition. Thampi *et al.* found an activity independent velocity-velocity correlation length, as found in the bulk flow measurements of Sanchez *et al.*, and studied defect dynamics in 2D simulations.

Here we construct a multi-scale model that identifies the sources of destabilizing active stresses, and study their consequences in large-scale simulations. We first perform detailed, hybrid Brownian dynamics-Monte Carlo (BD-MC) simulations which incorporate excluded-volume interactions between model MTs, thermal fluctuations, explicit motors with binding/unbinding kinetics that satisfy detailed balance, and a force-velocity relation. This model shows the generation of activity-driven extensile stresses from polarity sorting of anti-aligned MTs, and from crosslink relaxation of polar-aligned MTs. It also provides coefficients for polarity-specific active stresses for a kinetic theory that incorporates polarity sorting and long-range hydrodynamic interactions, using a similar approach as that used to describe bacterial suspensions<sup>13-16</sup>, where hydrodynamic instabilities lead to large-scale

collective motions including jets and vortices<sup>12,13,16–20</sup>. We use this model to study actively streaming nematic states on an immersed surface, as in the Sanchez *et al.* experiments. Numerical experiments demonstrate strikingly similar dynamics with large-scale turbulent-like fluid flows, and the persistent production and annihilation of defects. We correlate the defect dynamics with specific flow structures, and with active stresses. We identify the hydrodynamic instability of nearly 1D coherent “cracks” as being source of the persistent dynamics.

## I. THE MICROSCOPIC MODEL

Figure 1 outlines the basic physical picture that underlies both our BD-MC simulations and the continuum kinetic model. Consider an immersed suspension of polar MTs, each with a plus-end oriented director  $\mathbf{p}$ , and all of the same length  $l$  and diameter  $b$  (Fig. 1a). Adjacent MTs are coupled by active plus-end directed crosslinks consisting of two motors connected by a tether that responds as a spring to stretching (Fig. 1b). Motor velocities along an MT are controlled by a simple piecewise linear force-velocity relation. For a nematically aligned suspension there are two basic types of MT-MT interaction. For anti-aligned MTs (Fig. 1c) the motors of active crosslinks move in opposite directions, stretching the tether. This creates pulling forces on each MT that, acting against fluid drag, slide the MTs relative to each other towards their minus-ends. This process is termed *polarity sorting*<sup>5</sup>. Conversely, for polar-aligned MTs the cross-linked motors move in the same direction, there is little or no net sliding, and the tether pulling on the leading motor causes stretched tethers to relax (Fig. 1d).

## II. BROWNIAN DYNAMICS-MONTE CARLO SIMULATIONS

In our particle simulations, MTs are represented as rigid rods (discorectangles in 2D) of aspect ratio  $r = l/b$ . Forces and torques on MTs occur due to the crosslinks, particle-particle repulsion, anisotropic fluid drag, and thermal forces. The MTs’ short-range repulsive potential is the Weeks-Chandler-Andersen potential<sup>21</sup>; see Supplemental Material. There are no long-range hydrodynamic interactions. Without crosslinks, the thermodynamic properties of our system closely resemble those of hard rods, a well-characterized model in 2D<sup>22</sup>.

We assume a semi-grand canonical ensemble of noninteracting motors maintained in diffusive contact with MTs to which they can bind/unbind. When bound, crosslinks have a free energy  $u_c(r_c) = -u_0 + \frac{1}{2}Kr_c^2$ , where  $K$  is the crosslink spring constant and  $r_c$  is the extension between the crosslink endpoints. Crosslink attachment/detachment is a one-step process in which crosslinks bind to/unbind from two MTs simultaneously. The binding and unbinding rates are chosen to ensure that the correct equilibrium distribution of bound crosslinks is recovered for static (non-translocating) crosslinks, and for computational convenience (see Supplemental Material). Given the bound crosslinks, we compute the forces and torques exerted on the MTs by the crosslinks by differentiating  $u_c(r_c)$  with respect to the MT positions and orientations.

While bound, each motor translocates toward its MT plus-end with speed depending upon the force  $\mathbf{f}$  exerted by the crosslink (Fig. 1b). The force component parallel to the MT orientation vector  $\mathbf{p}$  (pointing to the plus-end) is  $f_{\parallel} = \mathbf{f} \cdot \mathbf{p}$ . Consistent with experiments<sup>23</sup>, we assume a piece-wise linear relation between  $f_{\parallel}$  and  $v$ :  $v = v_w \max(0, \min(1, 1 + f_{\parallel}/f_s))$ , where  $v_w$  is the maximum translocation velocity and  $f_s$  is the stall force. While the forces on the two motors are equal and oppositely oriented, their  $\mathbf{p}$  projections are not, and hence their translocation velocities are generally different.

The simulation scheme consists of BD steps alternating with kinetic MC sweeps. During each BD timestep, bound motors translocate toward MT plus-ends and MT positions and orientations are evolved under the forces and torques exerted upon them. Each MC sweep consists of a cycle of crosslink binding/unbinding trials. The procedure for crosslink binding is quite involved, because the rate of crosslink binding depends on crosslink extension, which in turn depends on the relative positions and orientations of the two MTs to which the crosslink is attached and on the motor attachment points.

The particle model depends on several dimensionless parameters. The crosslink concentration  $c$  controls crosslink interaction strength and activity. The motor speed  $v_w$  changes the overall level of activity in the system and alters two key dimensionless parameters, the *motor run length*  $\ell = v_w/(k_0l)$ , where  $k_0$  is a base binding rate, and the *Peclet number*  $Pe = v_w\eta b/k_B T$  (the ratio of translocation and diffusion rates, where  $\eta$  is the viscosity and  $k_B T$  is the Boltzmann constant times the temperature). While these and other parameters were varied in our study, most results presented here use  $\ell = 0.64$ , which sets the typical distance a motor travels during one binding event to be about the MT length. The MT

aspect ratio  $r$  was fixed at 10 (corresponding to monodisperse 250-nm-long MTs), and the MT volume fraction to  $\phi = 0.5606$ , which is a value where the system is nematic at equilibrium in the absence of crosslinks. More discussion of parameter choices and studies appears in the Supplemental Material.

**Extensile stress and its origins.** Figure 2 illustrates the long-time behavior of MT suspensions in the BD-MC simulation model. Fig. 2a shows a simulation of MTs interacting only through thermal fluctuations and steric interactions (without crosslinks). The system develops a 2D nematic state consistent with previous work<sup>22</sup>. Figure 2b shows the result of adding immobile crosslinks with full binding/unbinding kinetics. The system shows MT bundling due to short-range crosslink-induced attraction. Figure 2c shows the behavior when crosslinks actively translocate. The system now shows active MT flows driven by polarity sorting (see video1), leading to the formation of polar lanes (domains of MTs with similar polarity). These polar lanes are highly dynamic and show large fluctuations. The mean-squared displacement of MT position as a function of time shows diffusive behavior at long-times in the equilibrium cases (Figs. 2a and b) and for active MTs when measured perpendicular to the average alignment direction. For motion parallel to the average alignment direction, the active MT mean-squared displacement is superdiffusive and nearly ballistic at long times (Fig. 2d).

We have characterized the dynamical properties of bound crosslinks for polar-aligned and anti-aligned MT pairs. For two MTs labeled  $i$  and  $j$  with orientations  $\mathbf{p}_i$  and  $\mathbf{p}_j$  and center-of-mass displacement  $\mathbf{r}_{ij}$ , we define the pair's longitudinal displacement by  $s_{ij} = \frac{1}{2}\mathbf{r}_{ij} \cdot [\mathbf{p}_i + \text{sgn}(\mathbf{p}_i \cdot \mathbf{p}_j)\mathbf{p}_j]$ . For anti-aligned MT pairs ( $\mathbf{p}_i \cdot \mathbf{p}_j < 0$ ) undergoing crosslink-driven relative sliding,  $s_{ij}$  is negative when the MT pair is contracting (minus-ends closer than plus-ends), and becomes positive when the MT pair is extending (plus-ends closer than minus-ends; see Fig. 1). When crosslinks are immobile or for mobile crosslinks on polar-aligned MTs ( $\mathbf{p}_i \cdot \mathbf{p}_j \geq 0$ ), the distribution of crosslinks as a function of  $s_{ij}$  is symmetric (Fig. 2e). However for mobile crosslinks on anti-aligned MTs, the distribution of crosslinks skews toward positive values of  $s_{ij}$ : more crosslinks are bound during the extensile motion of the pair. This asymmetry occurs because of the translocation of the crosslinks toward the MT plus-ends. As a result, greater force is generated by the mobile crosslinks during pair extension, and this yields an extensile stress that drives active flows (see below).

The distribution of crosslink extension alters significantly when crosslinks can translocate

(Fig. 2f). The minimum value of  $r_c$  is approximately 1 due to excluded-volume interactions between MTs. For polar-aligned pairs, the distribution is shifted toward *smaller* extensions than in the equilibrium case due to nonequilibrium crosslink relaxation; this has important implications for the generation of extensile stress, as discussed below. For anti-aligned pairs, the distribution is shifted toward positive extension due to oppositely directed motor motion; this combination of crosslink extension and motion applies active forces that drive polarity sorting.

We measured the time-averaged bulk stress tensor  $\Sigma_b$  for our active particle system (see Supplemental Material), and find that, over a wide range of parameters,  $\Sigma_b$  is anisotropic with larger components in the average MT alignment direction than in the perpendicular direction. That is, since the MT alignment direction is essentially  $\hat{\mathbf{y}}$ , the stress difference  $N = \Sigma_b^{yy} - \Sigma_b^{xx}$  is positive, which corresponds to an extensile stress. Having static or no crosslinks (Fig. 2a, b) yields an isotropic  $\Sigma_b$ . The stress difference  $N$  can be expressed as the sum of pair interactions between nearby MTs, with each  $ij$  pair contributing a stresslet  $S_{ij}$  (with units of force $\times$ length), prior to division by the bulk volume. We have characterized how the stresslet varies with system parameters and configurations. The average pair stresslet  $S$  increases with the motor speed  $v_w$  up to a maximum where the typical motor run length is the MT length; see Fig. 2g. Increasing  $v_w$  further leads to decreasing  $S$  because the motors rapidly move to the ends of the MTs and unbind. To understand the sources of extensile stress, we studied how  $S$  varies with the local polar environment. For each MT  $i$  we define a polar orientational order parameter  $p_i$  which varies between 1 (if all neighboring MTs are polar-aligned to MT  $i$ ) and  $-1$  (if all neighboring MTs are anti-aligned to MT  $i$ ). In Fig. 2h we show a typical curve of  $S$  as a function of  $p_i$ .  $S$  is largest when  $p_i$  is near  $-1$ , suggesting that polarity sorting is the dominant source of pair-wise extensile stress. As  $p_i$  increases,  $S$  drops with approximate linearity, at least away from the two isolated peaks that close examination shows originating through strong steric interactions of nearly parallel MTs. Nearly, but not exactly, parallel MTs experience aligning torques due to crosslink-mediated attraction; the resulting steric collisions tend to promote pair extension that increases the extensile stress for nearly-aligned pairs (relative to perfectly aligned pairs).

The extensile stress from anti-aligned pair interactions arises from asymmetries during polarity sorting: if an MT pair begins sliding when the two minus-ends touch ( $s_{ij} = -10$ ) and slides under a force proportional to pair overlap until the two plus-ends meet ( $s_{ij} = 10$ ), then

the contractile motion would perfectly balance the extensile motion and the total extensile stress would be zero. In our simulations we observe two effects that break this symmetry. First, MTs are unlikely to begin interacting exactly when their minus ends are touching, decreasing the range of negative  $s_{ij}$  over which sliding occurs. Second, more motors are bound on average during extensional motion (so that  $s_{ij} > 0$ ; see Fig. 2e).

We also find the surprising and counterintuitive result that  $S$  remains positive even when  $p_i$  is near 1, that is, for polar-aligned pairs of MTs. This effect occurs due to an interplay between motor motion and excluded volume interactions. For perfectly parallel filaments, the effect can be understood by considering equilibrium *vs.* nonequilibrium crosslink relaxation. For immobile crosslinks, the system is at equilibrium and the stress tensor is isotropic; attractive interactions due to crosslinks are balanced by excluded volume interactions and thermal fluctuations, and the system is at mechanical equilibrium. When crosslinks are active, stress anisotropy becomes possible due to the force-velocity relation. In particular, the tether of a longitudinally stretched crosslink pulls back on the leading motor, slowing it, and pulls forward on the trailing motor. Hence, the crosslink relaxes its longitudinal extension. This effect is observable in Fig. 2e as a slight but significant shift in the distribution of crosslink extension toward smaller values relative to the equilibrium case. As a result, the crosslink-induced contractile stress along the MT alignment direction is decreased, while there is no change in the transverse stress induced by crosslinks. This leads to a net anisotropic extensile stress in the alignment direction. In this scenario, we would predict then that if the motors had a force-independent velocity, the polar-aligned extensile stress would vanish because the longitudinal crosslink extension would be unable to relax. We tested this prediction by studying how  $S$  varies as stall force increases for simulations of perfectly aligned (unable to rotate) isolated filament pairs. We find that the extensile stress changes little with stall force for anti-aligned MT pairs. However, for polar-aligned MT pairs the extensile stress drops as stall force increases and goes to zero for infinite stall force (which corresponds to force-independent velocity); see Fig. 2i. When effects of filament rotation are also included, the results are more subtle; we find that the interplay of filament rotation and crosslink activity can induce extensile stress for polar-aligned pairs in bulk simulations even for infinite stall force.

While the extensile stress due to polar-aligned MT pairs is typically a factor of 2–5 smaller than for anti-aligned pairs, when measured per pair (Fig. 2h), either polarity sorting, or the

tendency to form polar lanes (Fig. 2c), would mean the emergence of larger numbers of polar-aligned MT pairs than of anti-aligned. In our BD-MC simulations, which lack the effect of hydrodynamics, the overall contributions of polar-aligned and anti-aligned pairs to the extensile stress are comparable.

### III. CONTINUUM KINETIC THEORY

The BD-MC simulations show how polar-specific MT-pair interactions give rise to extensile bulk stresses. To study the effect of hydrodynamic interactions and to make analytical predictions we have developed a Doi-Onsager theory<sup>24</sup> similar to those used to describe the dynamics of motile rod suspensions<sup>13,14,16</sup>. The theory's fluxes and active stresses arise from polar-aligned and anti-aligned MT pair interactions produced by active crosslinks. These stresses induce chaotic flows driven by the formation of disclination defects.

To model this, the system is described by a distribution function  $\Psi(\mathbf{x}, \mathbf{p}, t)$  of MT center-of-mass positions  $\mathbf{x}$  and polar orientation vectors  $\mathbf{p}$  ( $|\mathbf{p}| = 1$ ), evolved through a Smoluchowski equation

$$\frac{\partial \Psi}{\partial t} + \nabla_x \cdot (\dot{\mathbf{x}}\Psi) + \nabla_p \cdot (\dot{\mathbf{p}}\Psi) = 0, \quad (1)$$

which reflects conservation of particle number. Here  $\dot{\mathbf{x}}$  and  $\dot{\mathbf{p}}$  are MT conformational fluxes. Important macroscopic quantities for describing a polar nematic system are the local concentration  $\Phi = \int_p \Psi$ , the local polarity vector  $\mathbf{q} = \int_p \Psi \mathbf{p} / \Phi$ , the second-moment tensor  $\mathbf{D} = \int_p \Psi \mathbf{p} \mathbf{p}$  which arises generically in capturing active stresses produced by active suspensions<sup>12</sup>, and the (trace-free) tensor order parameter tensor  $\mathbf{Q} = \mathbf{D} / \Phi - \mathbf{I} / d$ , with  $d = 2$  or  $3$  the spatial dimension.

To motivate our choice of particle fluxes, and to relate our model to the BD-MC simulations, we consider a nematically ordered local cluster of MTs undergoing polarity sorting (Fig. 1), with  $n$  MTs pointing rightwards (labelled  $R$ ) and  $m$  MTs pointing leftwards (labelled  $L$ ). Let all the MTs in this cluster be coupled by active crosslinks which create spring-like forces between the MTs, and whose bound ends move at a constant speed  $v_w$  toward MT plus-ends. For an anti-polar MT pair this induces a relative sliding, each towards its negative end. The cluster is assumed small enough so that all MTs experience the same local flow field. Using Stokesian slender body theory<sup>25</sup> we can find the velocities of the left-

and rightward pointing MTs (see Supplemental Material):  $v^L = \frac{2n}{n+m}v_w$ ,  $v^R = -\frac{2m}{n+m}v_w$ . This expression shows that the speed of each population depends on how many opposing MTs there are to pull against, with their drag as the anchor, and their relative velocity fixed at  $v^L - v^R = 2v_w$  by the motor protein speed. This latter observation is in agreement with observations of anti-aligned sliding of MTs in the mitotic spindle<sup>26</sup>.

Slender-body theory also yields the forces each rod exerts on the fluid, and hence the volume-averaged stress<sup>27</sup> by polarity sorting can be calculated. If the cluster occupies a volume  $V_c$ , the induced extra stress tensor from anti-aligned sorting is  $\Sigma_{aa} = \frac{\tilde{\eta}v_w l^2}{V_c} \frac{\alpha_1}{2} \frac{2mn}{m+n} \mathbf{pp}$ . Here  $\tilde{\eta}$  is proportional to fluid viscosity  $\eta$ , and  $\alpha_1 = s/l$  with  $s$  the signed distance between the center-of-masses of the  $\mathbf{p}$  and  $-\mathbf{p}$  oriented subclusters. If the cluster is extending then  $s < 0$ , as would be the case if motor-protein binding and unbinding kinetics biased crosslink densities towards the plus-end of the MTs. This is seen in the BD-MC simulations (Fig. 2e), and is associated with local extensile flows similar to those of motile Pusher particles which collectively can drive macroscopic flow instabilities<sup>13,16,28</sup>. The anti-aligned pair stresslet strength is  $S = \frac{\tilde{\eta}v_w l^2 \alpha_1}{m+n}$  with  $\alpha_1 \approx -2$  from the BD-MC simulations.

While active crosslinking between polar-aligned MTs yields little MT mobility, the BD-MC simulations show that it does yield an extensile stress. However, unlike polarity sorting we lack a simple first-principles model of how polar interactions yield extensile stress, though the number of polar pair interactions within a cluster scales as  $m^2 + n^2$ . Given that the anti- and polar-aligned stresses are of the same order (Fig. 2h) we assume the form  $\Sigma_{pa} = \frac{\tilde{\eta}v_w l^2}{V_c} \frac{\alpha_2}{2} \frac{m^2+n^2}{m+n} \mathbf{pp}$ . Comparison with the BD-MC simulations suggests that  $\alpha_2 \approx -0.5$ .

We have generalized this simple example to a continuum model that captures polarity sorting of MTs and the dependence of the stress upon the local polarity of the MT field. The fluxes for Eq. (1) are given in dimensionless form by

$$\dot{\mathbf{x}} = (\mathbf{q} - \mathbf{p}) + \mathbf{U} - D_t \nabla_x \ln \Psi, \quad (2)$$

$$\dot{\mathbf{p}} = (\mathbf{I} - \mathbf{pp}) (\nabla_x \mathbf{U} + 2\zeta_0 \mathbf{D}) \mathbf{p} - D_r \nabla_p \ln \Psi. \quad (3)$$

In Eq. (2),  $\mathbf{U}$  is the background fluid flow, and the last term yields translational diffusion with constant  $D_t$ . For nematically ordered suspensions, the term  $\mathbf{q} - \mathbf{p}$  exactly reproduces the cluster velocities induced by polarity sorting given above (note that for a perfectly polar system, no polarity sorting occurs and the flux  $\mathbf{q} - \mathbf{p}$  makes no contribution.) In Eq. (3), the MTs are rotated by the background flow gradient  $\nabla_x \mathbf{U}$  according to Jeffery's

equation<sup>29</sup> while the second term arises from the Maier-Saupe potential with coefficient  $\zeta_0$  which models torques and stresses arising from steric interactions at high concentration<sup>14,30</sup>. The last term yields rotational diffusion of the rod with constant  $D_r$ . In two-dimensions, the Maier-Saupe potential yields an isotropic to nematic phase transition, with increasing  $\zeta_0$ , when  $\zeta_0 = 4D_r$ . We do not account for MT rotation through interactions with the local field, as is appropriate when the MT field is nematically ordered. All constants have been made nondimensional using characteristic velocity  $v_w$ , and a characteristic length  $l_c$  appropriate for dense suspensions<sup>14,24</sup> (see Supplemental Material).

Our system is closed by specifying how  $\mathbf{U}$  and  $\nabla_x \mathbf{U}$  are recovered from  $\Psi$ , which involves specifying the extra stress created in the fluid by activity and other sources. We assume the active stress arises separately from anti-aligned and polar-aligned MT interactions, and construct it from  $\mathbf{D}$  and  $\Phi \mathbf{q} \mathbf{q}$  (i.e., the simplest symmetric tensors quadratic in  $\mathbf{p}$ ). In dimensionless form, the active stress tensor takes the form

$$\Sigma^a = \frac{\alpha_1}{2}(\mathbf{D} - \Phi \mathbf{q} \mathbf{q}) + \frac{\alpha_2}{2}(\mathbf{D} + \Phi \mathbf{q} \mathbf{q}). \quad (4)$$

The first term (second term) captures active stress production via polarity sorting (crosslink relaxation) and exactly reproduces the form of  $\Sigma_{aa}$  ( $\Sigma_{pa}$ ) for nematically ordered suspensions. The total extra stress tensor is given by  $\Sigma^e = \Sigma^a + \Sigma'$ , where  $\Sigma'$  models extra stresses arising from flow-induced constraint forces on MTs and steric interactions<sup>14</sup>(see Supplemental Material).

For bulk flow modeling one typically closes the system by balancing viscous and extra stresses and solving the forced Stokes equation  $-\nabla_x p + \Delta_x \mathbf{u} = -\nabla_x \cdot \Sigma^e$  and  $\nabla_x \cdot \mathbf{u} = 0$  with velocity  $\mathbf{u}$  and pressure  $p$ . This generates the background velocity and its gradient needed to evolve Eq. (1); e.g. see<sup>13</sup>. However, this approach does not describe the streaming nematic experiments of Sanchez *et al.*<sup>4</sup>, where the active material is confined to an interface between oil and water, so surface motions are coupled to external fluid motions. To capture that coupling, we consider a flat layer of interacting MTs bound in the  $xy$ -plane at  $z = 0$ , and immersed between two half-spaces filled with Newtonian viscous fluid (for simplicity, of the same viscosity). The activity in the MT layer generates a stress jump across the  $z = 0$  plane, and so generates a global 3D flow which is continuous at  $z = 0$ . We use the surface velocity  $\mathbf{U} = \mathbf{u}|_{z=0}$  and its surface gradient to drive the Smoluchowski equation. Using Fourier transforms in the  $xy$ -plane, the 3D homogenous Stokes equation for  $\mathbf{u}$  can be easily

solved with a stress jump and velocity continuous at  $z = 0$ . We further assume that the capillarity of the surfaces bounding the MT layer acts against concentration of MTs. This is accomplished through including a transverse pressure gradient within the MT layer and results in the background flow being incompressible in the plane. The surface flow is then neatly given as a velocity-stress relation in Fourier space:

$$\hat{\mathbf{U}} = \frac{i}{2}(\mathbf{I} - \hat{\mathbf{k}}\hat{\mathbf{k}})(\hat{\Sigma}^e\hat{\mathbf{k}}), \quad (5)$$

where  $\hat{\mathbf{k}} = \mathbf{k}/k$  is the normalized 2D wave-vector. It is useful to compare this expression to that for the 2D Stokes equation forced by a bulk stress:  $\hat{\mathbf{u}} = \frac{i}{k}(\mathbf{I} - \hat{\mathbf{k}}\hat{\mathbf{k}})(\hat{\Sigma}^e\hat{\mathbf{k}})$ . The missing factor of  $k^{-1}$  in Eq. (5) profoundly changes the nature of system stability for the surface *vs.* 2D bulk systems. Equation (5) not only closes the system but facilitates a pseudo-spectral method to solve the Smoluchowski equation (1) and the fluid flow in a coupled manner<sup>13</sup>.

**Flow, polarity and defects.** Assuming 2D periodic boundary conditions and using a Fourier pseudo-spectral numerical method, we have simulated our active polar nematic model, Eqs. (1-5), over long times. Simulating in regions of flow instability we find persistently unsteady flows that are correlated with continual genesis, propagation, and annihilation of  $\pm 1/2$  order defect pairs (see videos in Supplemental Material).

Figure 3 shows simulation results at late times, from initial data near uniform isotropy. Panel (a) shows the out-of-plane vorticity ( $\omega = V_x - U_y$ ; colorfield) overlaid by the surface velocity field  $\mathbf{U} = (U, V)$ . The dynamics are complex and appear turbulent (see video2), and qualitatively similar to those reported by Sanchez *et al.*<sup>4</sup>.

Figure 3b shows the corresponding nematic director field and scalar order parameter from the  $\mathbf{Q}$  tensor. The local orientation is highly correlated with the flow structures of panel a, and the surface is littered with  $\pm 1/2$  order defects which propagate freely about the system (see video3). These defects exist in regions of small nematic order (dark blue), and are born as opposing pairs in elongated “incipient crack” regions. These are associated with surface jets, locally decreasing nematic order, and increasing curvature of director field lines. Characteristically, the  $+1/2$  order defects approximately propagate away along their central axis and have a much higher velocity than those of  $-1/2$  order. The relatively higher surface velocity in the neighborhood of a  $+1/2$  order defect appears as a well-localized jet, in the direction of defect motion, between two oppositely signed vortices.

Figure 3c shows the “active force” vector field  $\mathbf{f}^a = \nabla_x \cdot \Sigma^a$  overlaying its magnitude. From

its definition one expects that its magnitude is correlated with regions of rapidly changing nematic order. Indeed, the panel reveals that large active force flows along an interconnected network of ridges that are correlated with the stringy regions of diminished nematic order and particularly with incipient cracks. Along such cracks the active force points in the direction from which newly nucleated  $+1/2$  order defects will emerge and propagate (see video4). Isolated high-force peaks correlate and move with  $+1/2$  order defects, again with the force pointing in the direction of their motion. Negative order defects are associated with regions of relatively lower force magnitude, likely due to the local symmetry of the nematic director field. We have also separated the two active stress contributions in Eq. (4) (not shown). The two stresses are large in complementary regions, with the “polar-aligned” (“anti-aligned”) stress large in regions of high (low) polar order. It is the anti-aligned stress that yields the largest forces, by about a factor of 3 (close to the ratio  $\alpha_1/\alpha_2$ ).

In Fig. 4 shows the nucleation and annihilation of defect pairs. Panel (a) shows the birth and separation of a defect pair, beginning from an incipient crack wherein the initially smooth director field (e.g., lower arrow in Fig. 3b) morphs into singular forms in regions of low nematic order. Typically the positively-signed defect moves away faster and roughly along its symmetry axis. Panel (b) shows the mutual annihilation of an oppositely-charged pair that, by chance, came into close proximity. Following their collision the nematic order increases as the director field reknits itself into a smooth form (e.g., upper arrow in Fig. 3b). Panel (c) contains both a defect and an incipient crack, overlaid by the polarity field  $\mathbf{q}$ . This shows that as the  $+1/2$  order defect propagates it leaves behind a region of increased polarity. Further, the polarity field rapidly rotates across the incipient crack (by approximately  $\pi/2$ ), and as sometimes occurs, forms a shock-like structure that precedes the birth of a new defect pair. Panel (d) plots the relative speed of the defect pairs in (a) and (b). The speeds are of the same order, and more importantly, on the order of the motor protein speed in our model (normalized to unity). This is consistent with experimental observations (*cf.* Fig. 3 of Sanchez *et al.*<sup>4</sup>). Finally, the dashed line plots the average fluid velocity around the defect pair which illustrates the general slowness of the surface flow in comparison to defect speeds. Hence, as is the case for defects in more standard liquid crystalline materials, the defects here are not material structures carried along by the background surface flow.

**Coherent structures and hydrodynamic instabilities.** A key observation from our simulations is that defect pairs are generated along elongated cracks that themselves de-

velop in regions of high polar order. We understand this as a concatenation of two linear instabilities. First, as shown in Supplemental Material, we can determine a nematically ordered homogeneous base-state by balancing angular diffusion against the aligning torque from steric interactions. By linearizing the Smoluchowski and momentum-balance equations around this base-state we can numerically calculate the growth-rates of plane-wave perturbations. This shows that the plane-wave vector of maximal growth is aligned with the nematic director ( $\theta = 0$  in Fig. 5a inset; also see<sup>13,14,16</sup>). Further, the analysis reveals a wave-number of maximal growth,  $k_{cr}$ , along this direction (Fig. 5a), with  $k_{cr}$  growing with approximate linearity in  $\alpha = \alpha_1 + \alpha_2$ . We note that in the 2D bulk model, maximal growth occurs at  $k = 0$ , and so does not produce a characteristic length-scale. However in this immersed layer system, long-wave growth is cut off (see discussion following Eq. (5)) and yields a finite length-scale of maximal growth.

The result of this instability is captured in nonlinear simulations by perturbing a MT suspension that is aligned along  $\hat{\mathbf{x}}$ . Figure 5b shows that a series of cracks form along  $\hat{\mathbf{y}}$ . These cracks are associated with up and down moving fluid jets, and bending of nematic field lines. In panel (b) inset, the spatial variations of the velocity field are seen to be in excellent agreement with the velocity eigenmode associated with  $k_{cr}$  for the linearized system. The distance between these cracks matches the half-wavelength, i.e.,  $\lambda_{cr} = \pi / k_{cr} \approx 10$ , which is in fact representative of the characteristic length between cracks seen in the full dynamics of motile defects (Fig. 3(b)). At late times (c) these cracks lose stability when interacting with each other, and are eventually terminated to form defect pairs reminiscent of pattern formation observed in other studies of active nematics<sup>31,32</sup>.

#### IV. DISCUSSION

We have developed an active-nematic theory to describe a suspension of MTs driven by the activity of plus-end directed motor-protein complexes. Detailed BD-MC simulations revealed polarity-sorting and polarity-specific active stresses. We incorporated these polarity-specific interactions into a kinetic theory of Doi-Onsager type, and studied the effect of hydrodynamic interactions. While we have a good understanding of the origin and dependencies of extensile stresses driven by polarity sorting, our understanding is less clear of the stress from polar-aligned interactions, and a reduced first-principles model of them

would be useful. Generally, increasing either  $\alpha_1$  or  $\alpha_2$  increases the number of defect pairs, which shortens the characteristic length-scale in the dynamics (see Fig. 5a). However, these two stresses arise from different polar arrangements of MTs. Fixing  $\alpha = \alpha_1 + \alpha_2$ , the case with  $\alpha_1 = 0$  (only polar-aligned active stress) produces more defects than does the case with  $\alpha_2 = 0$  (only anti-aligned active stress). Curiously, this seems due to the defects themselves, as the passage of a  $+1/2$ -order defect leaves behind it regions of higher polar order, and thence large bulk regions for polar-aligned interactions.

One apparent difference with the kinetic theory is the polar lanes observed in the BD-MC model, which lacks hydrodynamic coupling. To understand this we turned off hydrodynamics in the kinetic model and indeed find polar laning. Further, as revealed by linear theory, there is an instability to laning but it occurs on a much longer time-scale (as is also consistent with the BD-MC model) than the activity-driven instabilities studied here. It would be illuminating to compare the kinetic theory with BD-MC simulations that incorporate hydrodynamic interactions. This might be done using fast-summation methods applied earlier to the study of motile suspensions<sup>28,33</sup>.

Using this theory, we found a streaming-nematic state similar to that observed in recent experiments by Sanchez *et al.*<sup>4</sup>. We predict that defect pairs are born along incipient cracks of low nematic order, and that these cracks correlate with fluid jets. The movement of  $+1/2$  defect can be tracked by associated vortex pairs, and strongly correlates with the active force. We also identify a hydrodynamic instability of nearly-aligned MTs that causes formation of incipient cracks (see also Giomi *et al.*<sup>31</sup>), and hence serves as a source of complex dynamics. Further, linear theory for an immersed MT layer gives a characteristic length-scale for the dynamics which is likely related to Freedericksz lengths found in more coarse-grained active nematic models<sup>11,34</sup>.

While we have applied our polar active-nematic model to study these recent experiments, we believe that more elaborated kinetic models such as this might serve as a principled basis from which to study related biological systems such as the eukaryotic mitotic spindle.

*Acknowledgements.* We thank D. Chen, Z. Dogic, and D. Needleman for useful discussions. This work was funded by NSF grants DMR-0820341 (NYU MRSEC: TG,MJS), DMS-0920930 (MJS), EF-ATB-1137822 (MB), DMR-0847685 (MB), and DMR-0820579 (CU MRSEC: MG); DOE grant DE-FG02-88ER25053 (TG,MJS); NIH grant R01 GM104976-03

(MB,MJS); and the use of the Janus supercomputer supported by NSF grant CNS-0821794.

---

- <sup>1</sup> Nédélec, F., Surrey, T., Maggs, A. & Leibler, S. Self-organization of microtubules and motors. *Nature* **389**, 305–308 (1997).
- <sup>2</sup> Surrey, T., Nédélec, F., Leibler, S. & Karsenti, E. Physical properties determining self-organization of motors and microtubules. *Science* **292**, 1167–1171 (2001).
- <sup>3</sup> Schaller, V., Weber, C., Semmrich, C., Frey, E. & Bausch, A. Polar patterns of driven filaments. *Nature* **467**, 73–77 (2010).
- <sup>4</sup> Sanchez, T., Chen, D., DeCamp, S., Heymann, M. & Dogic, Z. Spontaneous motion in hierarchically assembled active matter. *Nature* **491**, 431–434 (2012).
- <sup>5</sup> Nakazawa, H. & Sekimoto, K. Polarity sorting in a bundle of actin filaments by two-headed myosins. *J. Phys. Soc. Japan* **65**, 2404–2407 (1996).
- <sup>6</sup> Kruse, K. & Jülicher, F. Actively contracting bundles of polar filaments. *Phys. Rev. Lett.* **85**, 1778–1781 (2000).
- <sup>7</sup> Kruse, K. & Jülicher, F. Self-organization and mechanical properties of active filament bundles. *Phys. Rev. E* **67**, 051913 (2003).
- <sup>8</sup> Liverpool, T. & Marchetti, M. Instabilities of isotropic solutions of active polar filaments. *Phys. Rev. Lett.* **90**, 13802 (2003).
- <sup>9</sup> Ahmadi, A., Marchetti, M. & Liverpool, T. Hydrodynamics of isotropic and liquid crystalline active polymer solutions. *Phys. Rev. E* **74**, 061913 (2006).
- <sup>10</sup> Giomi, L., Bowick, M., Ma, X. & Marchetti, M. Defect annihilation and proliferation in active nematics. *Phys. Rev. Lett.* **110**, 228101 (2013).
- <sup>11</sup> Thampi, S., Golestanian, R. & Yeomans, J. Velocity correlations in an active nematic. *Phys. Rev. Lett.* **111**, 118101 (2013).
- <sup>12</sup> Simha, R. & Ramaswamy, S. Statistical hydrodynamics of ordered suspensions of self-propelled particles: waves, giant number fluctuations and instabilities. *Phys. A* **306**, 262–269 (2002).
- <sup>13</sup> Saintillan, D. & Shelley, M. Instabilities and pattern formation in active particle suspensions: kinetic theory and continuum simulations. *Phys. Rev. Lett.* **100**, 178103 (2008).
- <sup>14</sup> Ezhilan, B., Shelley, M. & Saintillan, D. Instabilities and nonlinear dynamics of concentrated active suspensions. *Phys. Fluids* **25**, 070607 (2013).

- <sup>15</sup> Subramanian, G. & Koch, D. Critical bacterial concentration for the onset of collective swimming. *J. Fluid Mech.* **632**, 359–400 (2009).
- <sup>16</sup> Saintillan, D. & Shelley, M. Instabilities, pattern formation, and mixing in active suspensions. *Phys. Fluids* **20**, 123304 (2008).
- <sup>17</sup> Pedley, T. & Kessler, J. Hydrodynamic phenomena in suspensions of swimming microorganisms. *Ann. Rev. Fluid Mech.* **24**, 313–358 (1992).
- <sup>18</sup> Koch, D. & Subramanian, G. Collective hydrodynamics of swimming microorganisms: Living fluids. *Ann. Rev. Fluid Mech.* **43**, 637–659 (2011).
- <sup>19</sup> Sokolov, A., Goldstein, R., Feldchtein, F. & Aranson, I. Enhanced mixing and spatial instability in concentrated bacterial suspensions. *Phys. Rev. E* **80**, 031903 (2009).
- <sup>20</sup> Kurtuldu, H., Guasto, J., Johnson, K. & Gollub, J. Enhancement of biomixing by swimming algal cells in two-dimensional films. *Proc. Natl. Acad. Sci.* **108**, 10391–10395 (2011).
- <sup>21</sup> Weeks, J., Chandler, D. & Andersen, H. Role of repulsive forces in determining the equilibrium structure of simple liquids. *J. Chem. Phys.* **54**, 5237–5247 (1971).
- <sup>22</sup> Bates, M. & Frenkel, D. Phase behavior of two-dimensional hard rod fluids. *J. Chem. Phys.* **112**, 10034–10041 (2000).
- <sup>23</sup> Visscher, K., Schnitzer, M. & Block, S. Single kinesin molecules studied with a molecular force clamp. *Nature* **400**, 184–189 (1999).
- <sup>24</sup> Doi, M. & Edwards, S. *The theory of polymer dynamics*, vol. 73 (Oxford University Press, USA, 1988).
- <sup>25</sup> Keller, J. & Rubinow, S. Slender-body theory for slow viscous flow. *J. Fluid Mech.* **75**, 705–714 (1976).
- <sup>26</sup> Yang, G., Cameron, L., Maddox, P., Salmon, E. & Danuser, G. Regional variation of microtubule flux reveals microtubule organization in the metaphase meiotic spindle. *J. Cell Bio.* **182**, 631–639 (2008).
- <sup>27</sup> Batchelor, G. The stress system in a suspension of force-free particles. *J. Fluid Mech.* **41**, 545–570 (1970).
- <sup>28</sup> Saintillan, D. & Shelley, M. Emergence of coherent structures and large-scale flows in motile suspensions. *J. Roy. Soc. Int.* **9**, 571–585 (2012).
- <sup>29</sup> Jeffery, G. The motion of ellipsoidal particles immersed in a viscous fluid. *Proc. Roy. Soc. Lond. Ser. A* **102**, 161–179 (1922).

- <sup>30</sup> Maier, W. & Saupe, A. Eine einfache molekulare theorie des nematischen kristallinflüssigen zustandes. *Zeit. Nat. Teil A* **13**, 564 (1958).
- <sup>31</sup> Giomi, L., Mahadevan, L., Chakraborty, B. & Hagan, M. Excitable patterns in active nematics. *Phys. Rev. Lett.* **106** (2011).
- <sup>32</sup> Forest, M., Wang, Q. & Zhou, R. Kinetic theory and simulations of active polar liquid crystalline polymers. *Soft Matter* **9**, 5207–5222 (2013).
- <sup>33</sup> Saintillan, D., Darve, E. & Shaqfeh, E. A smooth particle-mesh Ewald algorithm for Stokes suspension simulations: The sedimentation of fibers. *Phys. Fluids* **17**, 033301 (2005).
- <sup>34</sup> Ramaswamy, S. The mechanics and statistics of active matter. *Ann. Rev. Cond. Matt. Phys.* **1**, 323–345 (2010).

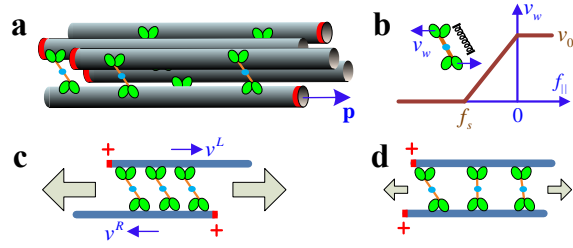


FIG. 1: (a) Schematic of a cluster of polar-aligned and anti-aligned MTs, with plus ends marked by red rings. Motors walk on neighboring MTs, and (b) exert spring-like forces. (c) An anti-aligned MT pair. (d) A polar-aligned MT pair. Grey arrows characterize the magnitude of the extensile stress.

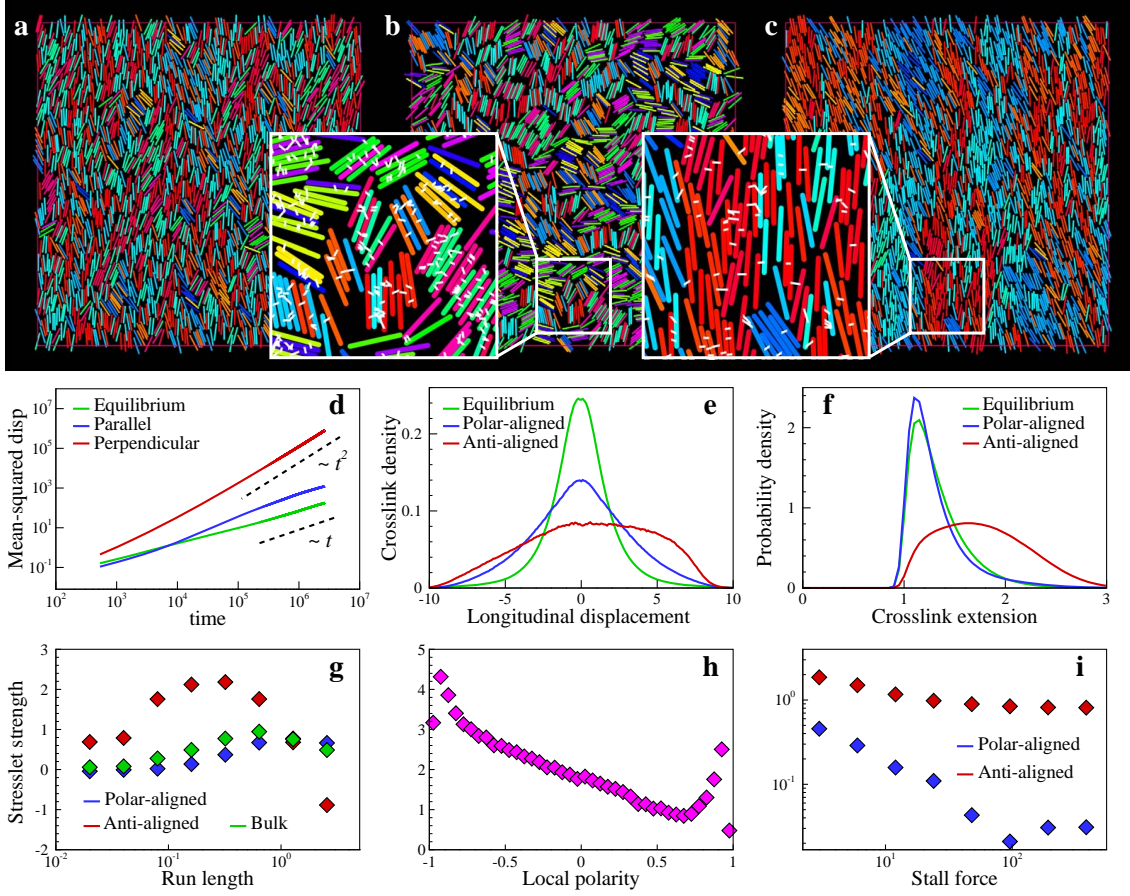


FIG. 2: (a-c) Snapshots of the BD-MC particle simulations. Rods are colored according to orientation, with a color wheel ranging through red (plus end down), green (left), blue (up), and purple (right). Insets are zoomed views with crosslinks explicitly shown in white. (a) System with no crosslinks, illustrating the 2D nematic state. (b) An equilibrium system with static crosslinks exhibits MT bundling due to short-range crosslink-induced attraction. (c) An active system with mobile crosslinks exhibits active flows and formation of polar lanes. (d) Mean-squared deviation of MTs as a function of time. (e) Histogram of crosslink occupancy as a function of the particle pair longitudinal displacement  $s_{ij}$ , broken into contributions from polar-aligned and anti-aligned pairs in the active case. (f) Histogram of crosslink extension  $r_c$ , broken into contributions from polar-aligned and anti-aligned pairs in the active case. (g) Variation of extensile pair stresslet  $S$  with motor run length  $\ell$ , showing results from the entire bulk simulation and contributions of polar-aligned and polar-antialigned pairs. (h) Variation of extensile pair stresslet with local polar environment  $p_i$ . (i) Variation of extensile pair stresslet with motor stall force from simulations of isolated, perfectly parallel filament pairs.

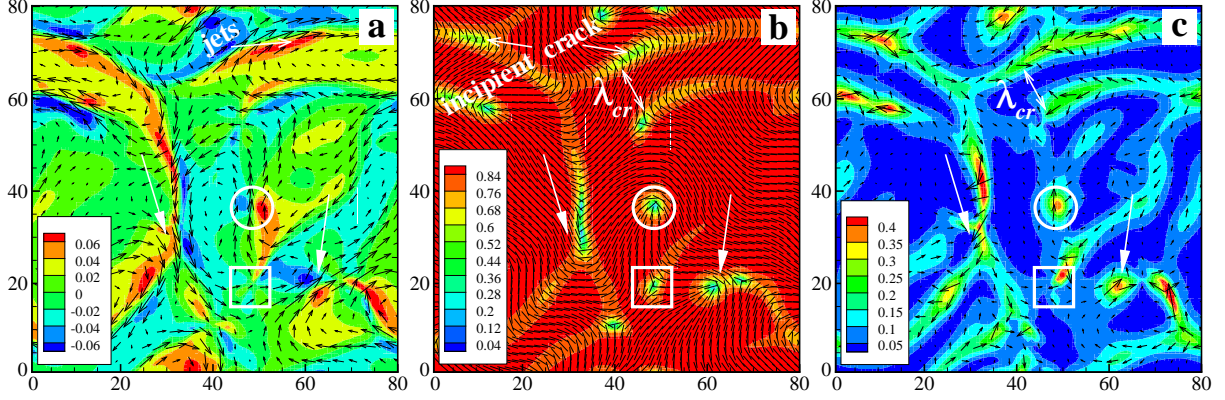


FIG. 3: Snapshots of streaming MT nematics on a liquid-liquid interface. (a) The background fluid velocity vector field superposed upon the contour map of the associated vorticity. (b) The nematic director field  $\mathbf{n}$  superimposed on the contour map of the scalar order parameter (twice the positive eigenvalue of the tensor  $\mathbf{Q}$ ). Disclination defects of order  $\pm 1/2$  appear in localized regions of low order. Here  $\lambda_{cr}$  represents a characteristic length between the cracks. (c) The vector field of the active force ( $\nabla \cdot \Sigma^a$ ), superimposed on its magnitude. In each panel, the position of a  $+1/2$ - and  $-1/2$ -order defect are marked by an open circle and square, respectively. The positions of one pair of annihilating defects are marked by a solid arrow at right, with the arrow at left identifying the “incipient crack” from which a defect pair is about to emerge. For all the simulations, we choose  $\alpha_1 = -2.0$ ,  $\alpha_2 = -0.6$ ,  $\beta = 1.74$ ,  $\nu = 0.5$ ,  $\zeta_0 = 1.0$ ,  $D_t = 0.5$  and  $D_r = 0.1$  (see Supplemental Material).

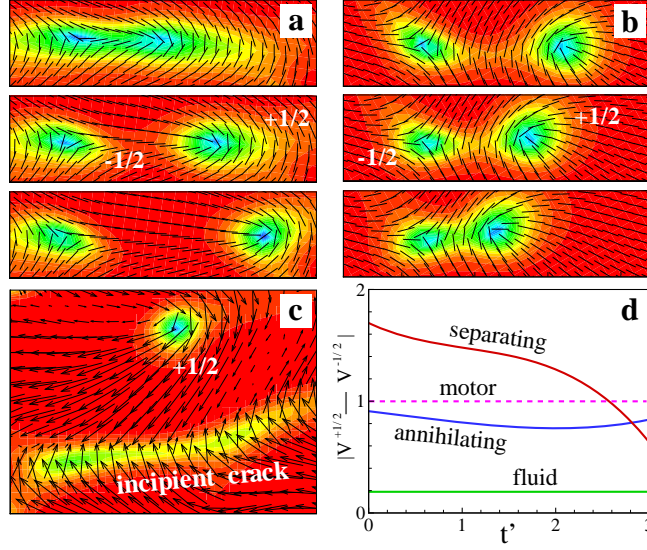


FIG. 4: Time sequential snapshots of the nematic director field  $\mathbf{n}$  for nucleation (a) and annihilation (b) of defect pairs. The (dimensionless) time spacing between frames is 5. (c) Polarity field associated with a motile  $+1/2$  disclination defect and an incipient fracture on the bottom. (d) Relative speed of the two oppositely charged defects, as well as the mean flow speed near this defect pair. In (a), (b) and (c), the contour map is the scalar order parameter, plotted with the same scale as Fig. 3b.

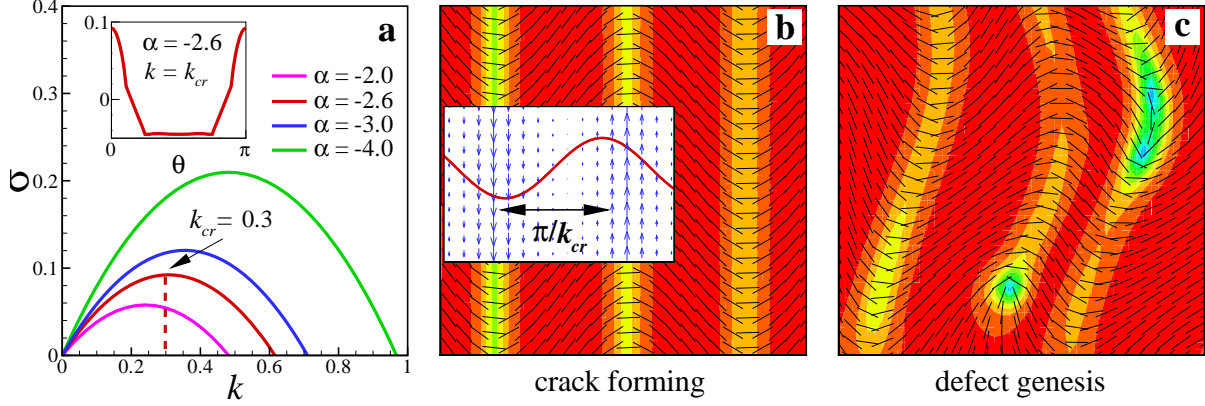


FIG. 5: Linear stability analysis (a) and nonlinear simulation (b,c) for strongly anti-aligned MTs. (a) The real part of the growth rate as a function of wave-number  $k$  for several  $\alpha$  ( $\alpha = \alpha_1 + \alpha_2$ ).  $k_{cr}$  corresponds to the maximum growth rate. Inset: real part of the growth rate as a function of wave-angle  $\theta$  when fixing  $k = k_{cr}$ . (b) Cracks formation. Inset: the fluid velocity vector field (blue) and the eigenmode (red line) associated with  $k_{cr}$  for the linear system. (c) Genesis of defects at late times. In (b) and (c), the nematic director field  $\mathbf{n}$  is plotted with the contour map of the scalar order parameter. The color scale is the same as Fig. 3b.